Dynamic morphoskeletons in development

Serra, Mattia; Streichan, Sebastian; Chuai, Manli; Weijer, Cornelis J.; Mahadevan, L.

Published in:
Proceedings of the National Academy of Sciences of the United States of America

DOI:
10.1073/pnas.1908803117

Publication date:
2020

Document Version
Peer reviewed version

Dynamic morphoskeletons in development

Mattia Serra[a], Sebastian Streichan[b,c], Manli Chuai[d], Cornelis J. Weijer[d], and L. Mahadevan[a,e,f,1]

[a]School of Engineering and Applied Sciences, Harvard University, Cambridge, MA 02138; [b]Kavli Institute of Theoretical Physics, University of California, Santa Barbara, CA 93106; [c]Department of Physics, University of California, Santa Barbara, CA 93106; [d]Division of Cell and Developmental Biology, College of Life Sciences, University of Dundee, Dundee DD1 5EH, UK; [e]Department of Organismic and Evolutionary Biology, Harvard University, Cambridge, MA 02138; [f]Department of Physics, and Kavli Institute for NanoBio Science and Technology, Harvard University, Cambridge, MA 02138

This manuscript was compiled on February 26, 2020

Morphogenetic flows in developmental biology are characterized by the coordinated motion of thousands of cells that organize into tissues, naturally raising the question of how this collective organization arises. Using only the kinematics of tissue deformation, which naturally integrates local and global mechanisms along cell paths, we identify the dynamic morphoskeletons behind morphogenesis, i.e., the evolving centerpieces of multi-cellular trajectory patterns. These features are model and parameter-free, frame-invariant, robust to measurement errors, and can be computed from unfiltered cell velocity data. It reveals the spatial attractors and repellers of the embryo by quantifying its Lagrangian deformation, information that is inaccessible to simple trajectory inspection or Eulerian methods that are local and typically frame-dependent. Computing these dynamic morphoskeletons in wild-type and mutant chick and fly embryos, we find that they capture the early footprint of known morphogenetic features, reveal new ones, and quantitatively distinguish between different phenotypes.

morphogenesis | cell motion | coherent structures | Finite Time Lyapunov Exponent

During embryonic development, cells undergo large scale coordinated motion during the process of tissue and organ formation that together shape the embryo. Understanding these processes requires integrating molecular, cellular and multi-cellular perspectives across a range of length and time scales, linking cellular-level gene expressions and regulatory signaling networks (1–4) to long-range intercellular interactions and mechanical force generation (5–8). These approaches are complemented by advances in live imaging techniques (9) that allow for the detailed tracking of cellular trajectories (10–14), providing exquisite geometric and kinematic information on tissue morphogenesis. Some natural questions that these experimental approaches raise include: Can one correlate cell position, cell velocity and cell-cell interactions with cell and tissue fate decisions? Can one link gene expression levels and cellular trajectories with active force generation to help unravel the biophysical basis for morphogenesis? Can one quantitatively analyze cell motion data to predict the ultimate outcomes of tissue morphogenesis and organ development in normal and pathological situations? Here we address the last question by providing a mathematically grounded framework to determine the evolving centerpieces of morphogenetic movements using experimentally determined cellular trajectories, thus providing an important step in bridging the gap between bottom-up mechanistic approaches and top-down statistical and computational approaches (15, 16) (Fig. 1a).

Minimally, any framework that aims to analyze spatio-temporal trajectories in morphogenesis requires a self-consistent description of cell motion that is independent of the choice of reference frame or parametrization. This frame-invariant description of cell patterns is termed objective (17), and ensures that the material response of a deforming continuum, e.g. biological tissue, is independent of the observer. To quantify this notion, we start by considering two coordinate systems used to describe cell flows: the first corresponding to $\mathbf{x} \in \mathbb{R}^3$ and a second one $\bar{\mathbf{x}}$ defined as $\bar{\mathbf{x}}(t) = \mathbf{Q}(t)\mathbf{x}(t) + \mathbf{b}(t)$ where $\mathbf{Q}(t), \mathbf{b}(t)$ are a time dependent rotation matrix and translation vector. A quantity is objective (frame invariant) if the corresponding descriptions in the $\mathbf{x}$ and $\bar{\mathbf{x}}$ transform according to specific rules (17). In particular, scalars must remain the same $\bar{c} = c$, vectors must transform as $\mathbf{x}$, and second order tensors as $\bar{\mathbf{A}} = \mathbf{Q}\mathbf{A}\mathbf{Q}^\top$. Taking the time derivative of $\bar{\mathbf{x}}$, $\dot{\bar{\mathbf{x}}}(t) = \dot{\mathbf{Q}}(t)\mathbf{x}(t) + \mathbf{Q}(t)\dot{\mathbf{x}}(t) + \dot{\mathbf{b}}(t)$, one can easily see that the velocity field and the streamlines, which are trajectories of the frozen velocity field, are frame dependent, i.e. any metrics based on them for comparative purposes are likely to be erroneous (Fig. 1b) owing to the inability to remove the dependence on artifacts associated with variations in the choice of reference frames etc.

Driven by the recent revolution in imaging morphogenetic flows and cellular movements (18, 19), a range of approaches have been developed to characterize mesoscopic cellular behavior. These include statistical tools based on the connectivity between neighboring sites (20), and methods quantifying cell shape changes and cell intercalation by mapping the temporal evolution of strain rates between neighboring cells (5, 6). However, because of the general time dependence of cell motion, any velocity or velocity gradient features such as streamlines or strain rates differ substantially from Lagrangian trajectory patterns that integrate over the history of particles motion.

As an illustrative example, consider the analytic veloc-

Significance Statement

Coordinated cell migration is a hallmark of tissue morphogenesis during development and emerges from the combination of local cell behaviors and distributed chemo-mechanical interactions integrated across many spatial and temporal scales. A challenge in the field is to predict developmental outcomes of tissue morphogenesis using cellular trajectories. We provide a rigorous kinematic framework to analyze cell motion and identify robust multi-cellular attractors and repellers in space and time. Our results yield a scheme for comparing different morphogenetic phenotypes and help bridge the gap between bottom-up and top-down modeling approaches to morphogenesis.

M.S., and L.M. designed the research study, M.S. performed the computations, S.S., M.C. and C.J.W. provided imaging datasets, M.S., S.S., C.J.W and L.M. analyzed and interpreted the results, and M.S. and L.M. wrote the paper.

The authors declare no conflict of interest.

[1]To whom correspondence should be addressed. E-mail: lmahadev@g.harvard.edu

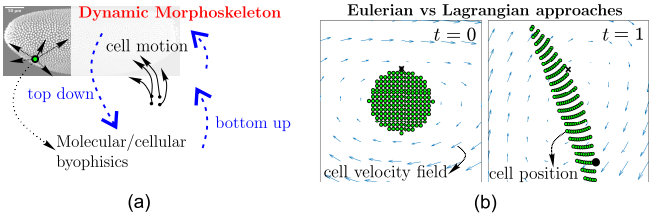

Fig. 1. (a) Sketch of bottom-up and top-down approaches to study cell motion. Bottom-up approaches study local mechanisms driving cells. Top-down approaches study patterns of cell motion caused by local and global driving mechanisms. The DM uncovers the centerpieces of cell trajectory patterns in space and time. (b) Snapshots of a simple analytic velocity field (blue) and its Lagrangian particle positions (green). The black dot marks the position of a particle started from the black x marker at time 0. The complete time evolution is available as Movie S1.

ity field $\mathbf{v}(\mathbf{x},t) = (x_1 \sin 4t + x_2(2+\cos 4t) + 0.2x_1x_2)\mathbf{e_1} + (x_1(\cos 4t - 2) - x_2 \sin 4t + 0.3x_1x_2)\mathbf{e_2}$, whose objective rate of strain tensor $\mathbf{S}(\mathbf{x},t)$ has components $S_{ij} = (\partial v_i/\partial x_j + \partial v_j/\partial x_i)/2$. Figure 1b shows that the frame-dependent velocity field (blue) suggests a vortex-type structure, while Lagrangian particles (green) correctly reveal the presence of exponentially-stretching deformations. Even if one averages the objective dominant rate of strain eigenvalue at a fixed (Eulerian) location marked by the black x over a time interval $[0,1]$, this average completely ignores the Lagrangian positions (black dot) explored by a trajectory starting from the x marker at time 0. Using explicit formulas relating Eulerian and Lagrangian deformations, in the SI we show that local changes of tissue flows can lead to global effects, which are detectable only by a Lagrangian analysis. This simple example and observations show that Eulerian methods, regardless of their objectivity, are inherently suboptimal for studying cellular flows, and suggest that a frame-invariant Lagrangian method is more suitable to assess global flows such as those seen in morphogenesis.

Here, we use the notion Lagrangian Coherent Structures (21), initially derived to study fluid flow patterns, to create an objective kinematic framework for analyzing cell motion. This allows us to uncover the dynamic morphoskeletons underlying morphogenesis, which quantify Lagrangian tissue deformations and correspond to the attracting and repelling organizers of cell trajectories in space and time. We illustrate our results on wild-type and mutant embryo imaging datasets obtained by light-sheet microscopy (LSM) in the context of primitive streak formation in the chick and early gastrulation in the fly.

Defining the dynamic morphoskeleton using Lagrangian coherent structures

In general, trajectories of time dependent dynamical systems have complicated shapes, are sensitive to changes in their initial conditions, and are characterized by multiple spatial and temporal scales. However, underlying these complicated paths, one often finds a robust skeleton that organizes the spatiotemporal structures in the dynamical system - referred to as Lagrangian Coherent Structures (LCSs) (21), which shapes trajectory patterns and provides a simplified description of the overall dynamics. They involve information obtained by integrating the trajectories in space-time and thus serve as a memory trace of the dynamical system. They can be defined for large or small time spans (22). In a general setting, we

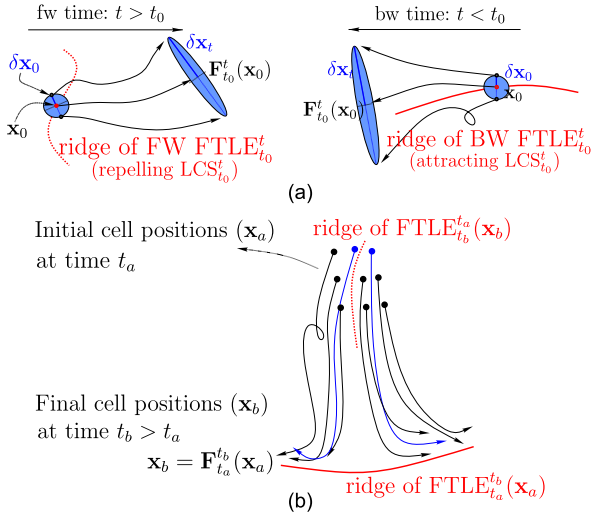

Fig. 2. (a) The $FTLE^t_{t_0}(\mathbf{x}_0)$ measures the maximum separation ($\sim |\delta\mathbf{x}_t|/|\delta\mathbf{x}_0|$) induced by the flow at $\mathbf{x}_0$ over the time interval $[t_0,t]$ between two initially close points in the neighborhood of $\mathbf{x}_0$. A forward time FTLE ridge - a set of points with high FTLE values - marks a repelling LCS whose nearby points from opposite sided of the ridge will experience the maximum separation over $[t_0,t], t > t_0$. Similarly, a backward time FTLE ridge demarcates an attracting LCS, i.e., a distinguished curve at t_0 which has attracted initially distant particles over $[t,t_0], t < t_0$. (b) Illustration of attracting and repelling LCSs over a time interval of interest $[t_a,t_b]$, $t_b > t_a$, during which cells move from their initial configuration $\mathbf{x}_a$ to their final one $\mathbf{x}_b = \mathbf{F}^t_{t_0}(\mathbf{x}_a)$. The forward FTLE is a scalar field over $\mathbf{x}_a$ while the backward FTLE over $\mathbf{x}_b$. Blue trajectories show cells that start close to each other from opposite sides of a repelling LCS, and end up far apart along the same attracting LCS.

schematize this in Fig. 2 and illustrate the impact of attracting and repelling LCSs on trajectory patterns over a time interval $[t_0,t]$. The combined effect of attracting and repelling LCSs is shown in Fig. 2b. For example, blue trajectories represent two cells that were initially very close (blue dots) but end up far apart. Even though they end up far apart, and hence are apparently subject to very different fates, they end up on the same attracting LCS after separating from a repelling LCS. Therefore, assessing the system through individual trajectories, despite being Lagrangian, will return poor results.

While there are a number of methods to determine Lagrangian (i.e., with memory) Coherent Structures (23), the Finite Time Lyapunov Exponent (FTLE), despite its limitations (21), remains the most used because it is computationally simple. The FTLE is characterized by a scalar field used to locate regions of high separation (or convergence) of initially close (distant) particles over $[t_0,t]$. Denoting by $\mathbf{v}(\mathbf{x},t)$ a velocity field obtained from imaging data, the induced Lagrangian flow map $\mathbf{F}^t_{t_0}(\mathbf{x}_0)$ is given by

$$\mathbf{F}^t_{t_0}(\mathbf{x}_0) = \mathbf{x}_0 + \int_{t_0}^{t} \mathbf{v}(\mathbf{F}^\tau_{t_0}(\mathbf{x}_0),\tau)\, d\tau, \qquad [1]$$

which maps the initial positions (of cells, membranes or nuclei, for example) $\mathbf{x}_0$ at time t_0 to their final positions at time t. The FTLE is then defined as

$$FTLE^t_{t_0}(\mathbf{x}_0) = \frac{1}{|T|} \ln \left(\max_{\delta\mathbf{x}_0} \frac{|\overbrace{\nabla\mathbf{F}^t_{t_0}(\mathbf{x}_0)\delta\mathbf{x}_0}^{\delta\mathbf{x}_t}|}{|\delta\mathbf{x}_0|} \right), \qquad [2]$$

where $|\cdot|$ represents the absolute value and ∇ the Jacobian with respect to $\mathbf{x}_0$. The FTLE is thus a measure of the maximum separation rate between a trajectory starting at $\mathbf{x}_0$ and a neighboring one starting at $\mathbf{x}_0 + \delta\mathbf{x}_0$, over $[t_0, t]$ (Fig. 2a) (see SI for explicit formulas for computing Eq. (2)).

We note that the FTLE depends on the base time t_0, the spatial location $\mathbf{x}_0$ - which correspond to the positions of Lagrangian particles at the base time - and the final time t, which sets the time scale $T = t - t_0$. As illustrated in Fig. 2a, a set of points $\mathbf{x}_0$ with high forward FTLE values (FW FTLE ridge) marks a region at t_0 whose neighboring particles from opposite sides of the ridge will get repelled achieving maximum separation at the later time $t = t_0 + T,\ T > 0$. Similarly, a backward FTLE ridge marks regions that at the base time t_0 have attracted initially distant particles over the time interval $[t_0 + T, t_0],\ T < 0$. Together, the FW and BW FTLE fields associated with varying time scales T uncover the exact spatial locations of repelling and attracting LCSs, along with the times at which they appear and cease to exist. We further note that over a time interval of interest $[t_a, t_b],\ t_b > t_a$ during which cells move from their initial configuration $\mathbf{x}_a$ to their final one $\mathbf{x}_b = \mathbf{F}_{t_a}^{t_b}(\mathbf{x}_a)$, the FW FTLE is a scalar field over $\mathbf{x}_a$ while the BW FTLE is a scalar field over $\mathbf{x}_b$. Therefore, over $[t_a, t_b]$, trajectories initially at opposite sides of FW FTLE ridges will be repelled from each others and get attracted to BW FTLE ridges by time t_b (Fig. 2b).

A mechanical interpretation of Eq. (2) follows by noting that the $\mathrm{FTLE}_{t_0}^{t}(\mathbf{x}_0)$ is proportional to the logarithm of the highest eigenvalue $\lambda_2(\mathbf{x}_0)$ of the Cauchy–Green strain tensor $\mathbf{C}_{t_0}^{t}(\mathbf{x}_0) = [\nabla\mathbf{F}_{t_0}^{t}(\mathbf{x}_0)]^{*}\nabla\mathbf{F}_{t_0}^{t}(\mathbf{x}_0)$ (17), a naturally invariant measure of deformation of a continuous medium. Hence it represents the maximum deformation induced by the flow over $[t_0, t]$ on an infinitesimal area element centered at $\mathbf{x}_0$ (Fig. 2a), and thus provides an exact link between the DM and the Lagrangian strain experienced by cells during morphogenesis. Separation or convergence of cell trajectories captured by the FTLE can arise from a combination of isotropic (volume or area) changes – due e.g., to cell divisions, ingression and area change – and anisotropic (shear) deformations – due to cell shape changes and cell intercalation. To quantify these two effects, we define the percentage of Lagrangian attraction due to anisotropic deformations over $[t, t_0], t < t_0$ as

$$A_{t_0}^{t} = \frac{\sqrt{\lambda_2} - \sqrt[4]{\det \mathbf{C}_{t_0}^{t}}}{|\sqrt[4]{\det \mathbf{C}_{t_0}^{t}} - 1| + \sqrt{\lambda_2} - \sqrt[4]{\det \mathbf{C}_{t_0}^{t}}}\%, \qquad [3]$$

where we dropped the $\mathbf{x}_0$ dependences (SI, Methods). The same formula in forward time ($t > t_0$) quantifies the percentage of anisotropic repulsion. Therefore, Eqs. (2-3) completely quantify and characterize tissue deformations. We now deploy these concepts on two paradigmatic problems in large scale morphogenetic flows: primitive streak (PS) formation in the chick embryo and gastrulation in the whole fly embryo. In both cases, we will follow the spatiotemporal evolution of the DM in terms of the FTLE fields as a function of their memory T, and thus determine the attracting and repelling manifolds underlying tissue organization. We also compare the DM and the overall Lagrangian deformations in wild-type and mutant phenotypes.

Results

Primitive streak (PS) formation in chicken embryo. The PS is a hallmark of bilateral symmetry in many organisms, is the site of ingression of the mesoderm and endoderm precursors and involves large scale cell flows to form an axial structure that serves to organize embryogenesis. The formation of this structure is best understood in the chick embryo and involves coordinated flow of more than 100,000 cells in the epiblast. Here we generate a cell velocity dataset of a Myr-GFP embryo using a dedicated LMS as described in (24). The velocity field is defined on a uniform rectangular grid of size $[4.77mm \times 3.14mm]$ over a time interval of approximately $12h$ from the freshly laid egg (stage EGK-XII) (25) to HH4 (26), prior to the onset of tissue movement, with spatial resolutions of $0.65\mu m$ and temporal resolution of $3min$. As in (24), we filtered the cell velocities using a centered averaging filter with a 5×5 spacial, and a $5-$time instances temporal window sizes. Movie S2 shows the velocity field overlaid over the experimental fluorescence images of the epiblast surface. We then compute attracting and repelling LCSs as BW and FW FTLE (SI, Methods) for a set of time scales $|T|$ spaced by $20min$.

Figure 3a left shows the FW FTLE_0^{12h}, indicating the presence of two repellers. The first repeller demarcates the boundary between the embryonic and extra-embryonic area. The second repeller, in contrast, demarcates a sharp boundary within the embryonic region. The right panel shows the BW FTLE_{12h}^{0}, highlighting the presence of an attractor that corresponds to the formed PS. Passively transporting with $\mathbf{F}_{12h}^{0}$ the BW FTLE field, which is based at final ($12h$) cell configuration to the initial time ($0h$), we identify the initial set of the mesendoderm precursor cells (yellow region bounded by the black level set in Fig. 3a center) that will finally form the PS. We overlay repeller two on this plot, and marking cells on its different sides in magenta and green we show that it sharply divides the A and P parts of the PS, as confirmed by the final cell positions. From Movie S3, which shows a sequence of panel (a) for different $|T|$, we observe that repeller two forms around $|T| = 400min$.

It is well established that cells in the anterior and posterior streak differentially express key genes code for important signals and signal modulators and that cells in various parts of the streak have different fates (27–29). Several of these genes are initially expressed in sickle shaped regions in the early streak stage embryo, however their expression domains separate during the streak extension (Fig. S4). This suggests that repeller two is a dynamic structure associated with the separation of gene expression domains and a functional readout of cell fate during streak formation, the mechanistic basis for which needs to be investigated in future experiments. For comparison, Movie S3 also shows the averaged velocity field, the evolution of a dense set of points, and the deformation of an initially uniform grid that moves with the flow. Remarkably, repellers remain entirely hidden to these tools. The attractor, instead, cannot be detected by the average velocity diagnostic and becomes visible to the dense set of points and the deforming gird when the PS is already formed. Although the latter two diagnostic are Lagrangian, they do not use the deformation gradient $\nabla\mathbf{F}$ but just the deformation $\mathbf{F}$, hence requiring longer time compared to the FTLE for identifying attractors. While embryonic regions towards which cells tend to cluster have been studied before (16, 24), our analysis pre-

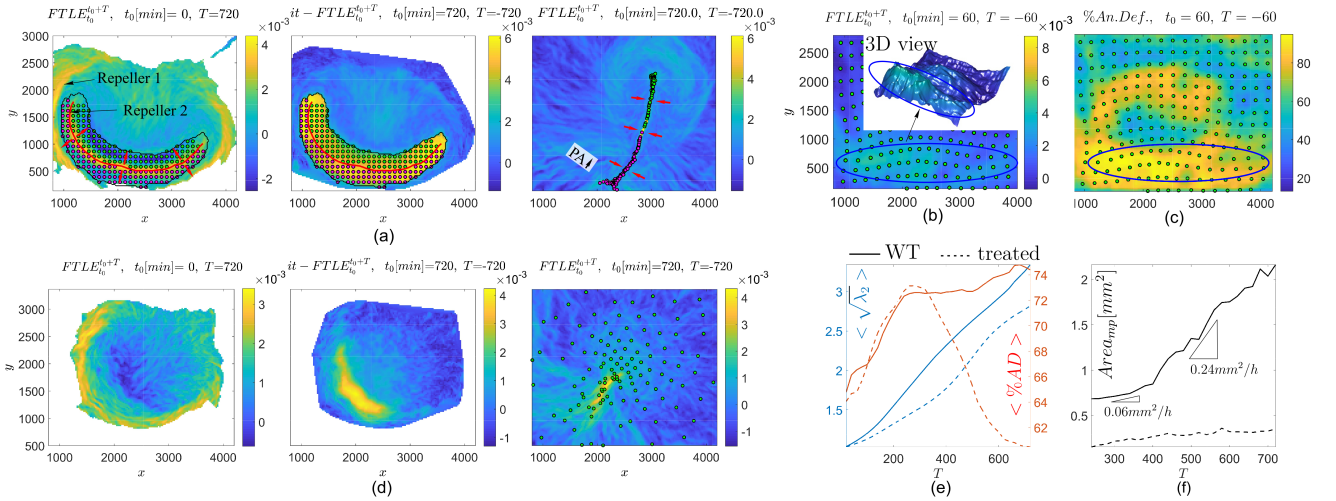

Fig. 3. (a) Left: FW FTLE corresponding to the full dataset highlights two repelling LCSs. Right: BW FTLE corresponding to the full dataset highlights the attracting LCS corresponding to the formed PS. Center: BW FTLE field in Right passively transported by $\mathbf{F}^0_{12h}$ to the initial time marks the initial position of the mesendoderm precursor cells, bounded by the solid black line, that will finally form the PS. Cells starting at different sides of repeller two will form the anterior and posterior part of the PS. White areas correspond to regions where the FTLE is unavailable because trajectories left the domain over which the velocity field is defined. The FTLE has unit $\min^-1$, the axis units are in μm. The time evolution of the FTLE fields and cell positions for different T is available as Movie S3. (b) The BW FTLE ridge (attracting LCS) for $T = 1h$ highlights the early footprint of the PS (blue ellipse) using only data within $[0, 1]h$ during which cells (green dots), initially released on a uniform rectangular grid, barely moved. (c) The A field associated with the left panel shows that the cell convergence in the early PS formation is dominated $\geq 80\%$ by anisotropic deformations. (d) Same as (a) for a chick embryo treated with an FGF receptor inhibitor. Movie S4 shows the time evolution of the FTLE fields and cell positions for different T. (e) Lagrangian tissue deformation quantified as the spatially averaged $\sqrt{\lambda_2}$ (blue), where λ_2 denotes the highest eigenvalue of $\mathbf{C}_0^T(\mathbf{x}_0)$. Red curves show the associated averaged % of anisotropic deformation. (f) Quantification of the initial area of the mesendoderm precursor cells that will form the PS (Fig. 3 (a) center) computed automatically from the FTLE field, as explained in Fig. S6.

cisely locates in space and time also repelling regions that are key in shaping multicellular patterns and studying cell fate.

Remarkably, already within $60min$, while cells barely moved, the BW FTLE already shows a footprint of the PS forming perpendicularly to the AP direction encircled by a blue ellipse in Fig. 3b. Differently from existing studies, where the early location of the PS is obtained by following backward in time the cells belonging to the formed PS (24), our approach does not use future data, hence revealing the footprint of PS formation only from Lagrangian deformations. Figure 3c shows the $A^t_{t_0}$ field associated with panel (b), highlighting that the Lagrangian attraction giving rise to the early PS footprint is dominated ($\geq 80\%$) by anisotropic deformations. In Fig. S5 and Movie S11, we show a comparison of the BW FTLE, the isotropic Lagrangian convergence, the velocity divergence and the $A^t_{t_0}$. This analysis highlights that the BW FTLE and the $A^t_{t_0}$ completely capture and quantify the PS formation and tissue deformations, both of which remain hidden to the Lagrangian and Eulerian isotropic convergence fields.

FGF (fibroblast growth factor) signalling is required for the early specification of mesendoderm and early gastrulation movements the chick embryo (30, 31). Figure 3d shows the same analysis as (a) for a chick embryo treated with $1\mu M$ of an FGF receptor inhibitor (LY2874455), which was added at $t = 84min$ (32). We find that the overall size of the attractor region is smaller compared to the wild type, consistent with the FGF treatment. We see that repeller two is absent in the treated embryo, implying that development is inhibited before the functional differentiation of A and P streak cells takes place. Movie S4 shows Fig. 3d for different T. As an aggregate measure of Lagrangian tissue deformation, we consider the spatial average of $\sqrt{\lambda_2}$ which measures the ratio of the deformed ellipse major semiaxis to the initial radius of the undeformed infinitesimal circle. Figure 3e shows that after the first $\approx 4h$, the tissue deformation of the WT embryo is $\approx 20\%$ higher compared to the PTB one. By contrast, the average percentage of anisotropic deformation in the two cases is similar in the first $\approx 4h$ and then remains dominant $\geq 72\%$ in the WT while rapidly decreasing to $\approx 60\%$ in the FGF-treated embryo indicating a key role for FGF signalling in the maintenance of cell-cell intercalation. While these changes are considerable, further work is required to study their statistics across embryos. In Fig. 3f, we quantify the area of mesendoderm precursor cells at the initial time (Fig. 3a center) that will finally form the PS. We identify the solid black curve delimiting the area automatically from the FTLE field, as described in Fig. S6. The WT embryo area is three times bigger than the treated one before $400min$, which corresponds to the formation of repeller two. After that, the WT area increases at a rate four times higher than before, leading to a final area six times bigger than the FGF-treated embryo.

In Fig S7, we show the same analysis of Fig. 3a using the raw unfiltered velocity. We find that the DM is exceptionally robust to noise and measurement errors, and is perfectly computable without ad-hoc filtering cell velocities.

Gastrulation in the fly embryo. Instead of focusing only on a specific morphogenetic feature, here we analyze the early development of the entire fly embryo. During gastrulation of Drosophila, about 6000 cells on the embryonic blastoderm on the embryo surface undergo global morphogenetic flow which induce severe tissue deformation, finally giving rise to the three germ layers. We compute the DM on an "ensemble averaged" cell velocity dataset from 22 wild-type (WT) Drosophila

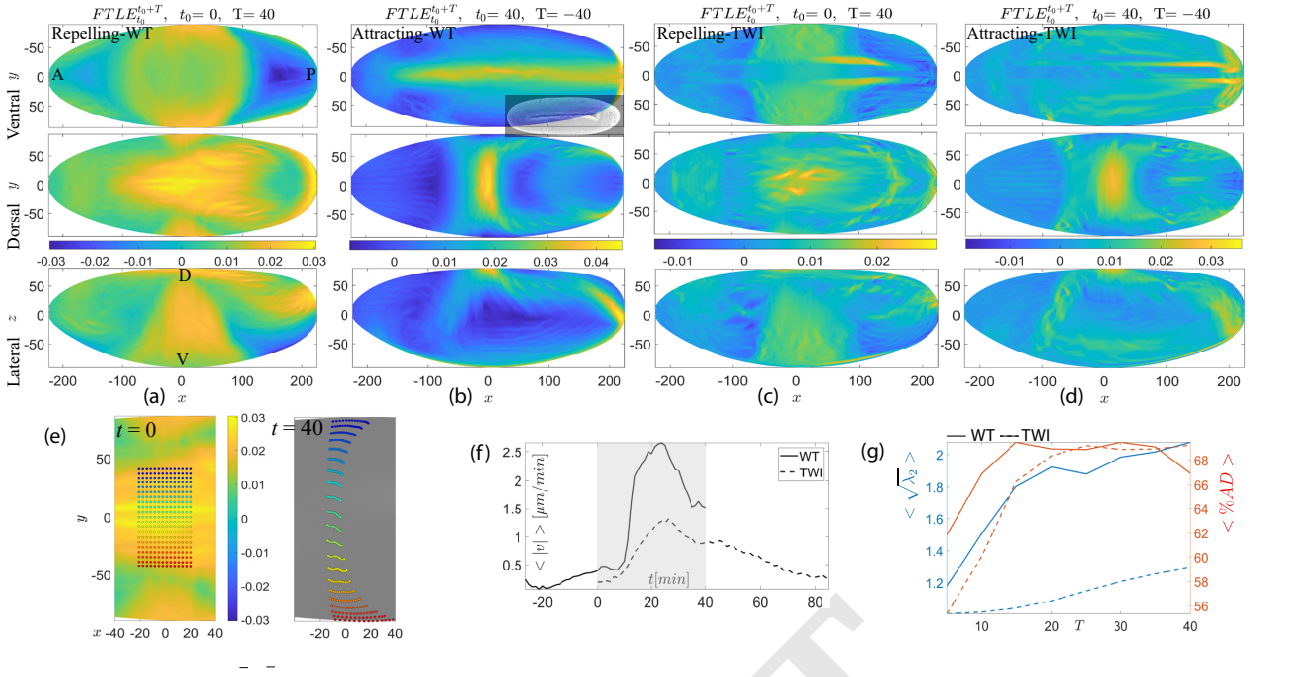

Fig. 4. (a) The FW FTLE$_0^{40}$ highlights two main repellers in the WT embryo. The FW FTLE evolution for different T is available as Movie S5. The FTLE has unit $\min^-1$ and the axis units are in μm. (b) The BW FTLE$_{40}^0$ highlights the attracting LCSs in the WT embryo. The inset shows the VF from an embryo image obtained by LSM. The time evolution of BW FTLE for different T is available as Movie S6. Movie S7 is the same as Movie S6 along with cells position in green. (c) Same as (a) for an ensemble averaged TWI mutant embryo. Movie S8 shows the FW FTLE for different T. (d) Same as (b) for an ensemble averaged TWI mutant embryo. Movie S9 shows the BW FTLE for different T along with cell positions. (e) Effect of the ventral repeller in panel (a) top on nearby cells (see Fig. S8a for a detailed analysis). (f) Spatially averaged speed of WT and TWI ensemble averaged datasets. The gray area indicates the region of the analysis, and time 0 coincides with the first appearance of the cephalic furrow from LMS images. (g) Lagrangian tissue deformation quantified as the spatially averaged $\sqrt{\lambda_2}$ (blue). Red curves show the associated averaged anisotropic deformation contributions.

melanogaster embryos undergoing gastrulation (33). Each velocity dataset is obtained combining in toto light sheet microscopy (11, 12) and tissue cartography (34), and consists of coarse-grained velocities averaged with a spatial window of ≈5 cell size. The velocity field is given on 1800 grid points over the fixed apical embryo surface (Fig. S1), and covers a time interval of forty minutes with a temporal resolution of $75sec$, starting right after cephalic furrow (CF) formation. In the SI-Methods we provide the formulas for computing FTLE induced by cell motion on curved surfaces.

We compute the DM for a set of time scales $|T|$ spaced every $5min$. Figure 4a shows the FW FTLE$_0^{40}$ in the WT embryo. The diffuse high FTLE pattern on the lateral side marks the lateral region that will undergo high stretching during germband extension (GBE) (compare with cell trajectories in Movie S7). The D pole repeller highlights a highly deforming area perpendicular to AP, and the P pole repeller marks a second region of distinct high deformation during GBE. Figure 4e shows the effect of the dorsal repeller on nearby cells. We perform a detailed analysis of the dorsal and posterior pole repellers in Fig. S8, and show that FTLE provides an accurate time-scale dependent map of Lagrangian deformations and cell repulsion. Movie S5 shows the FW FTLE field for different T.

Movie S6 shows the BW FTLE field for different T whose last ($T = 40$) frame corresponds to Fig. 4b, and highlights three main attractors. The ventral furrow (VF) attractor forms around $t = 10$, the dorsal one around $t = 20$ and the U-shaped attractor close to the P pole at $t = 25$, which demarcates the posterior-lateral boundaries of the GBE. On the dorsal side, drosophila gastrulation is characterized by several transverse structures which include the already formed CF, the anterior and posterior folds, and the posterior midgut invagination. Given the coarse-grained nature of the velocity field, structures whose width is smaller than 5 cell size, such as the CF and the transverse folds, should not be visible. The combined effect of the anterior and posterior folds, and the posterior midgut invagination, however, results in the strong transverse dorsal attractor that slightly moves from posterior to anterior marking the dorsal boundary of the GBE. Movie S7 shows the BWFTLE along with cells position confirming the role of the attractors and repellers in shaping cell motion.

We performed the same analysis on an ensemble-averaged dataset from seven twist (TWI) mutant embryos (33). Time $0min$ of WT and TWI datasets coincides with the first appearance of the CF from LMS images. Figure 4f shows the spatially average speed of the two datasets and the gray box indicates the time of our analysis when both WT and TWI velocities are available. Figures 4(c-d) show the same as (a-b) for the TWI dataset. Twist embryos lack the VF attractor, as expected, and also show more diffused and weaker dorsal and posterior pole attractors compared to WT (compare b and d). The dorsal repeller is also significantly weaker and smaller than in the WT (compare a and c center). Interestingly, the TWI embryo has two marked ventral repellers symmetric to the AP axis, which are not present in the WT. These repellers mark regions of cell separation induced by shear deformations, as shown in Fig. S9. In Fig. 4g, we show that the overall tissue deformation, quantified as described above, is ≈ 60% higher in the WT than in the TWI embryo within the first $40min$ from CF formation, while the corresponding anisotropic

deformation is the dominant contribution ($\geq 66\%$) in both. Although WT and TWI embryos genetically differ only locally in the ventral region where twist is expressed, such difference quickly induces global changes, which are promptly captured by the DM that shows marked differences also in the dorsal region. By contrast, the velocity field topology looks similar in WT and TWI datasets (Movie S10) except for the VF region during VF formation. We give a mathematical explanation of this difference in SI - Methods C. These results reaffirm that local morphogenetic changes can induce global effects, which are precisely quantified by our approach. Finally, comparing Movie S10 with Fig. 4 reinforces that the dynamic morphoskeletons reveal the key organizers of cell motion and quantify tissue deformations, both of which remain hidden to Eulerian velocity plots.

Conclusions

Using only available kinematic data associated with cell trajectories, we have provided a systematic kinematic framework for analyzing morphogenetic flows to uncover the evolving centerpieces of cell trajectory patterns which we term the Dynamic Morphoskeleton (DM). The DM is frame invariant and based on a Lagrangian description of tissue deformation captured by the FTLE, which naturally combines local and global mechanisms along cell paths. The DM is composed of attracting and repelling LCSs towards which cells converge to, or diverge from, over a specific time scale. Of particular note is evidence not just for attracting regions, but repelling regions that are just as important in determining cell fate. As aggregate measures, we have defined the overall Lagrangian tissue deformation and the corresponding isotropic and anisotropic fractions.

We have also shown that the DM provides information that is inaccessible to existing methods such as the velocity field topology, simple inspection of cell trajectories and deforming Lagrangian grids. In the cases we have studied, the DM either coincides with known morphogenetic structures and identifies their early footprints, or reveals new ones which invariably shape trajectory patterns. In the chick PS formation, we have found that already within $1h$ from freshly laid egg, the DM identifies the footprint of cells that will be part of the primitive streak. Additionally, we have found a repeller that separates the AP cells within the primitive streak, and related it to gene expression patterns. Overall, comparing their DM and aggregate deformation measures, we have found that our approach quantitatively distinguishes wild type and pathological embryos in both chick and fly morphogenesis.

Since the DM is driven solely by kinematic information, it is computable from cell motion data and is agnostic to the mechanisms generating them. This is both an advantage and a disadvantage - as it provides a framework to study the organizers of development, and yet does not shed light on their origin. On the one hand, owing to its Lagrangian nature, we expect that the DM can help to quantify the relative importance of co-existing spatiotemporal mechanisms in morphogenesis. But to make it even more powerful, a natural next step is to connect the DM to known gene expression patterns and mechanical processes, as well as identify new ones by performing targeted experiments to manipulate attractors and repellers.

Data Availability. The data and numerical codes are available upon request from the corresponding author.

ACKNOWLEDGMENTS. We thank Antti Karjalainen and Ricardo Bango Da Cunha Correira for their contribution in generating the chicken embryo datasets, and Matteo Rauzi, Adam Martin and Yogesh Goyal for helpful discussions. We are also grateful to the anonymous reviewers for their insightful suggestions. M.S. acknowledges support from the Schmidt Science Fellowship. C.J.W acknowledges support from the grant BBSRC BB/N009789/1.

1. Irvine K, Wieschaus E (1994) Cell intercalation during Drosophila germband extension and its regulation by pair-rule segmentation genes. *Development* 120(4):827–841.
2. Leptin M (1995) Drosophila gastrulation: from pattern formation to morphogenesis. *Annu Rev Cell Dev Biol* 11(1):189–212.
3. Zallen J, Wieschaus E (2004) Patterned gene expression directs bipolar planar polarity in Drosophila. *Developmental cell* 6(3):343–355.
4. Martin A, Kaschube M, Wieschaus E (2009) Pulsed contractions of an actin–myosin network drive apical constriction. *Nature* 457(7228):495.
5. Blanchard G, et al. (2009) Tissue tectonics: morphogenetic strain rates, cell shape change and intercalation. *Nature methods* 6(6):458.
6. Butler LC, et al. (2009) Cell shape changes indicate a role for extrinsic tensile forces in Drosophila germ-band extension. *Nature Cell Biology* 11(7):859.
7. Lye C, et al. (2015) Mechanical coupling between endoderm invagination and axis extension in Drosophila. *PLoS biology* 13(11):e1002292.
8. Irvine K, Shraiman B (2017) Mechanical control of growth: ideas, facts and challenges. *Development* 144(23):4238–4248.
9. Keller PJ (2013) Imaging morphogenesis: technological advances and biological insights. *Science* 340(6137):1234168.
10. Keller PJ, Schmidt AD, Wittbrodt J, Stelzer EH (2008) Reconstruction of zebrafish early embryonic development by scanned light sheet microscopy. *science* 322(5904):1065–1069.
11. Krzic U, Gunther S, Saunders TE, Streichan SJ, Hufnagel L (2012) Multiview light-sheet microscope for rapid in toto imaging. *Nature methods* 9(7):730.
12. Tomer R, Khairy K, Amat F, Keller PJ (2012) Quantitative high-speed imaging of entire developing embryos with simultaneous multiview light-sheet microscopy. *Nature methods* 9(7):755.
13. Amat F, et al. (2014) Fast, accurate reconstruction of cell lineages from large-scale fluorescence microscopy data. *Nature methods* 11(9):951.
14. Wolff C, et al. (2018) Multi-view light-sheet imaging and tracking with the MaMuT software reveals the cell lineage of a direct developing arthropod limb. *eLife* 7.
15. Oates AC, Gorfinkiel N, Gonzalez-Gaitan M, Heisenberg CP (2009) Quantitative approaches in developmental biology. *Nat. Rev. Genet.* 10(8):517.
16. Gross P, Kumar KV, Grill SW (2017) How active mechanics and regulatory biochemistry combine to form patterns in development. *Annual review of biophysics* 46:337–356.
17. Truesdell C, Noll W (2004) *The non-linear field theories of mechanics*. (Springer).
18. Royer L, Lemon W, Chhetri R, Keller P (2018) A practical guide to adaptive light-sheet microscopy. *Nat Protoc* 13(11):2462.
19. McDole K, et al. (2018) In toto imaging and reconstruction of post-implantation mouse development at the single-cell level. *Cell* 175(3):859–876.
20. Graner F, Dollet B, Raufaste C, Marmottant P (2008) Discrete rearranging disordered patterns, part I: Robust statistical tools in two or three dimensions. *The European Physical Journal E* 25(4):349–369.
21. Haller G (2015) Lagrangian coherent structures. *Annual Rev. Fluid. Mech* 47:137–162.
22. Serra M, Haller G (2016) Objective Eulerian coherent structures. *Chaos* 26(5):053110.
23. Hadjighasem A, Farazmand M, Blazevski D, Froyland G, Haller G (2017) A critical comparison of Lagrangian methods for coherent structure detection. *Chaos* 27(5):053104.
24. Rozbicki E, et al. (2015) Myosin-II-mediated cell shape changes and cell intercalation contribute to primitive streak formation. *Nat Cell Biol* 17(4):397.
25. Eyal-Giladi H, Kochav S (1976) From cleavage to primitive streak formation: a complementary normal table and a new look at the first stages of the development of the chick: I. general morphology. *Developmental biology* 49(2):321–337.
26. Hamburger V, Hamilton HL (1951) A series of normal stages in the development of the chick embryo. *Journal of morphology* 88(1):49–92.
27. Yang X, Dormann D, Münsterberg AE, Weijer CJ (2002) Cell movement patterns during gastrulation in the chick are controlled by positive and negative chemotaxis mediated by fgf4 and fgf8. *Developmental cell* 3(3):425–437.
28. Hatada Y, Stern CD (1994) A fate map of the epiblast of the early chick embryo. *Development* 120(10):2879–2889.
29. Alev C, et al. (2010) Transcriptomic landscape of the primitive streak. *Development* 137(17):2863–2874.
30. Chuai M, et al. (2006) Cell movement during chick primitive streak formation. *Developmental biology* 296(1):137–149.
31. Hardy KM, Yatskievych TA, Konieczka J, Bobbs AS, Antin PB (2011) Fgf signalling through ras/mapk and pi3k pathways regulates cell movement and gene expression in the chicken primitive streak without affecting e-cadherin expression. *BMC developmental biology* 11(1):20.
32. Zhao G, et al. (2011) A novel, selective inhibitor of fibroblast growth factor receptors that shows a potent broad spectrum of antitumor activity in several tumor xenograft models. *Molecular cancer therapeutics* 10(11):2200–2210.
33. Streichan S, Lefebvre M, Noll N, Wieschaus E, Shraiman B (2018) Global morphogenetic flow is accurately predicted by the spatial distribution of myosin motors. *eLife* 7:e27454.
34. Heemskerk I, Streichan SJ (2015) Tissue cartography: compressing bio-image data by dimensional reduction. *Nature methods* 12(12):1139.